Aerosol direct radiative impact over the INDOEX area based on passive and active remote sensing

J.-F. Léon, P. Chazette, Jacques Pelon, F. Dulac, H. Randriamiarisoa

Aerosol direct radiative impact over the INDOEX area based on passive and active remote sensing

J.-F. Léon,[1,3] P. Chazette,[1] J. Pelon,[2] F. Dulac,[1] and H. Randriamiarisoa[1]

Received 1 November 2000; revised 3 April 2001; accepted 21 August 2001; published 17 August 2002.

[1] This study is dedicated to the direct radiative impact assessment of the pollution aerosol particles during the Indian Ocean Experiment (INDOEX). We use here an instrumental synergy based on active and passive ground-based (Goa University, India), airborne (Mystere 20 research aircraft), and spaceborne (Meteosat-5) devices. An original method based on ground-based active actinic flux measurements is developed to assess the atmospheric, columnar aerosol single scattering albedo. This parameter has been found between 0.88 and 0.93 (at 440 nm) with an absolute uncertainty of 0.04 during the operating period from 11 to 23 March 1999. We have also assessed this parameter off the West Indian coast by comparing simultaneous airborne lidar and flux measurements with radiative transfer simulations. The value retrieved for the atmospheric column is close to 0.83 ± 0.05 (at 523 nm) in agreement with the coastal value. The horizontal and vertical extent of the aerosol plume is investigated using airborne lidar and Meteosat-5 satellite. Using the Meteosat-5-derived aerosol optical thickness, we have estimated the regional extent of the shortwave aerosol direct radiative forcing. The vertical profile of the aerosol extinction coefficient derived from lidar sounding is used to assess the atmospheric shortwave heating rate induced by the aerosol layer. For an aerosol optical thickness of 0.6 ($\pm$0.12), as it has been observed in the aerosol plume in late March, the top of atmosphere direct aerosol forcing is -17 ($\pm$5) W m^{-2}. The surface forcing is between 2.5 and 4.5 higher than the top of atmosphere forcing. This difference leads to a significant heating of the three lowest kilometers of the atmosphere by the aerosols. For an aerosol optical thickness of 0.6, the atmospheric heating rate induced by aerosols is between 0.8 and 1.2 Kd^{-1} depending on the aerosol single scattering albedo value. *INDEX TERMS:* 0305 Atmospheric Composition and Structure: Aerosols and particles (0345, 4801); 0345 Atmospheric Composition and Structure: Pollution—urban and regional (0305); 3359 Meteorology and Atmospheric Dynamics: Radiative processes; 3360 Meteorology and Atmospheric Dynamics: Remote sensing

1. Introduction

[2] Atmospheric aerosols are of paramount importance in the Earth's radiative budget because of their ability to increase scattering and absorption of shortwave (solar) radiation [*Charlson et al.*, 1992] and to impact cloud microphysics [*Twomey et al.*, 1984]. Impact of aerosols on the long wave radiation could be also significant but is much smaller than the solar forcing. At the opposite of greenhouse gases climate forcing, aerosols are thought to exert a cooling influence on climate [e.g., *Charlson et al.*, 1992; *Kiehl and Briegleb*, 1993; see also *Haywood and Boucher*, 2000, and references therein]. Assessing this influence is made complex by the high spatial and temporal variability of aerosol physical, chemical, and optical properties and geographical distribution, due to different sources and short atmospheric residence times. Atmospheric aerosols are affected by human activities through injection of complex mixtures of primary solids particles such as mineral dust and graphitic carbon, and of secondary substances such as sulfates, nitrates, and organic matter into the atmosphere. Since most of the anthropogenic aerosols are submicron particles, the optical depth of the aerosol layer decreases with increasing wavelength so the aerosol layer tends to be transparent at thermal wavelengths [*Harshvardhan*, 1993]. Their main radiative effect is then confined to solar wavelengths. In addition to their potential effect on the top of atmosphere shortwave radiative balance, aerosols may have a significant impact on the energy budget of the atmospheric layer in which they are [*Alpert et al.*, 1998], as well as on the surface below [*Fouquart et al.*, 1987]. The aerosol enhances the radiative cooling at the surface while the lower atmosphere may be affected by a significant heating in case of absorbing aerosols. It can then result in a change in the characteristics of the turbulent fluxes of sensible or latent heat.

[3] The estimation of the additive direct and indirect radiative impact of anthropogenic aerosols is the main purpose of the Indian Ocean Experiment (INDOEX) which

[1]Laboratoire des Sciences du Climat et de l'Environnement, CEA-CNRS, Gif/Yvette, Cedex, France.
[2]Service d'Aéronomie, CNRS-UPMC, Paris, France.
[3]Now at LOA, CNRS-USTL, 59655, Villeneuve d'Ascq, France.

0148-0227/02/2000JD000116

intensive field phase (IFP) took place in the North Indian Ocean (NIO) between January and March 1999. During the winter monsoonal months January through April, airflow over the NIO is dominated by transport from Indian and south Asian subcontinent. This northeastern flow carries out a significant loading of anthropogenic aerosols [*Satheesh et al.*, 1999] over the NIO where high aerosol optical thickness has been observed [*Léon et al.*, 2001]. The absorption observed in the aerosol plume results mainly from carbon originating from biomass burning and fossil fuel combustion, and with a smaller contribution from mineral dust [*Satheesh et al.*, 1999; *Schwartz and Buseck*, 2000]. A key parameter for the estimation of the direct radiative impact of aerosols is the albedo for single scattering quantifying the ratio between scattering and extinction, i.e., scattering plus absorption. Single scattering albedo is far from being a conservative property. It depends on the relative source strengths of the various aerosol substances and on the aging occurring during transport.

[4] In an effort to assess the direct radiative impact of the aerosols observed in the NIO, we present in this paper measurements dedicated to the evaluation of the aerosol optical parameters. On the one hand, aerosol optical parameters (optical thickness, single scattering albedo, and phase function) are derived from ground-based optical measurements performed at the Goa University experimental site (S. C. Alfaro et al., Variability of aerosol size resolved composition at an Indian coastal during the Indoex intensive field phase, submitted to *Journal of Geophysical Research*, 2002, hereinafter referred to as Alfonso et al., submitted manuscript, 2002) [*Léon et al.*, 2001]. More precisely, we develop an original method which permits to assess the columnar integrated single scattering albedo. On the other hand, we derive the horizontal and vertical distribution of the aerosol plume spreading over the NIO from satellite remote sensing and airborne lidar profiling, respectively. Finally, we estimate the shortwave direct radiative forcing and the atmospheric heating rate over the NIO associated to the observed haze.

2. Instrumentation

[5] During the IFP, a set of instruments dedicated to measurements of aerosol physical, chemical, and optical properties has been set up at a coastal site in India. This site is mainly influenced by northeasterly airflow during the winter monsoonal months (approximately from December to April). The experimental site located at the Goa University (15° 48′N, 73.°08′E) is bounded by the ocean on its western side and by the Western Ghat mountain range (700 m above sea level) on its eastern side about 50 km in the East of Goa. Measurements from this site have already been exploited to characterize aerosol physical, chemical, and optical properties. From ground based sampling (particle sizing and chemical analysis), an aerosol model was built up by S. C. Alfaro et al. (submitted manuscript). This model proved to be coherent with other results established in the NIO [e.g., *Satheesh et al.*, 1999]. Moreover, using a ground-based lidar and a Sun photometer at the Goa station in addition with Meteosat remote sensing of aerosols, *Léon et al.* [2001] have shown that the Goa site, thanks to its particular location, is well suited to describe the characteristics of the aerosols inside the Indian plume over the NIO.

[6] In this work we use three instruments set up at the Goa station during the IFP: an automatic Sun tracking photometer, an integrating nephelometer, and an optical actinometer. In addition, the regional scale characterization of the plume is realized thanks to measurements acquired by the meteorological satellite Meteosat-5 and the airborne lidar Leandre-1 on board the French research aircraft Mystere-20.

2.1. Ground-Based Measurements

2.1.1. Sun Photometer

[7] A Sun tracking photometer (manufactured by Cimel Electronics, Paris, France) was operated at the Goa University from mid-December to the early April 1999 [*Léon et al.*, 2001]. The spectral extinction of the direct solar beam was measured at four wavelengths (440, 670, 865, and 1020 nm) in a 1.2° field of view [*Holben et al.*, 1998]. The calibration of the instrument is performed by use of the method developed by *Herman et al.* [1981].

2.1.2. Nephelometer

[8] At the Goa surface station, we operated a three-wavelength integrating nephelometer (manufactured by TSI inc.,USA) which includes backscatter features (see also *Veefkind et al.* [1996]) between 10 March and 25 March. This instrument provides pseudo-total-scattering (integration of the scattering function for scattering angles between 7 and 170°) and pseudo-backscattering (between 90 and 170°) coefficients of an aerosol sample illuminated in the sampling chamber by a halogen light source. The light scattered by the aerosol is split into three wavelengths (450, 550, and 700 nm, respectively) using high-pass and band-pass color filters in front of the photo-multiplier tube detectors. We do not use the 550 nm channel which data are relatively noisy due to a failure in the detection chain.

2.1.3. Optical Actinometer

[9] The actinic flux is sensitive to aerosol presence and is a function of the aerosol optical parameters. To monitor the actinic flux at the ground station, we operated a JNO2 optical actinometer (manufactured by Metcon, Glashütten, Germany). It is dedicated to the measurement of the photodissociation rate coefficient $J(NO_2)$ of NO_2 molecule. $J(NO_2)$ is a function of the actinic flux, the photodissociation quantum yield and the absorption cross section of the NO_2 molecule. Actinic flux is measured by a radiometer made up of two identical detectors with uniform response over 2π sr. Using the calibration coefficient performed with a chemical actinometer, the measured actinic flux is directly converted into $J(NO_2)$ values (in s^{-1}) with a relative accuracy of about 1%. Both detectors were set up at about 6 meters above the ground, one pointing up and the second one parallel but pointing down. Such a configuration allows the determination of the upward $J(NO_2)^{up}$ and downward contribution $J(NO_2)^{dn}$. This instrument was operated at the Goa university from 25 February to 25 March. Due to a failure of the downward detector, only 4 days with simultaneous $J(NO_2)^{up}$ and $J(NO_2)^{dn}$ are available. $J(NO_2)$ data are recorder every 5 min.

2.2. Airborne Measurements

[10] The French research aircraft Mystere-20 (M20) was equipped with remote sensing instruments composed of

upward and downward viewing visible radiometers complemented by the backscatter lidar LEANDRE-1 [*Pelon et al.*, 1990]. The backscattering lidar LEANDRE-1 was installed onboard M20 to make observations of the aerosol vertical structure and optical properties at a wavelength of 532 nm. The bandwidth is 0.5 nm. The channel operating at 1064 nm was not used due to problems with the detection system. Simultaneous measurements were performed by passive radiometry for the analysis of solar flux scattered by the transported aerosols. Downward and upward shortwave radiative fluxes at the top of the aerosol layer have been measured by means of two Eppley pyranometers (broad band radiometers from 0.3 to 2.8 μm) located above and below the aircraft.

2.3. Spaceborne Measurements

[11] Satellite observations of the sunlight reflected by the Earth-atmosphere system enables the retrieval of the vertically integrated tropospheric aerosol content over oceanic surfaces in terms of aerosol optical thickness [*Kaufman et al.*, 1997]. Many previous studies were dedicated to quantitative observations of dust outbreaks [e.g., *Fraser*, 1976]. Studies have been made using Meteosat observations in the solar visible spectrum (using the VIS channel) to retrieve the desert aerosol optical thickness over the tropical North Atlantic [*Jankowiak and Tanré*, 1992] and the Mediterranean Sea [*Dulac et al.*, 1992]. Meteosat offers the unique opportunity of monitoring the aerosol load at synoptic and hourly scales. Thanks to the shift by the European Meteorological satellite agency (Eumetsat) of the Meteosat-5 satellite previously operated at 0° longitude to a position close to 63° E, this monitoring has become possible over the INDOEX area.

3. Aerosol Characteristics: Methods and Results

[12] Assessing the radiative impact of an aerosol layer requires the assessment of the structural and optical aerosol parameters. Regarding the top of atmosphere shortwave radiative forcing, many approximate analytical solutions linking the shortwave forcing and the aerosol optical properties were given [*Charlson et al.*, 1992; *Kiehl and Briegleb*, 1993; *Chylek et al.*, 1995; *Russel et al.*, 1997]. The aerosol optical parameters involved in these expressions are the aerosol optical thickness, the fraction of radiation scattered by aerosols into the upper hemisphere and the aerosol single scattering albedo. The fraction of radiation scattered by aerosols into the upper hemisphere is directly related to the aerosol phase function. Those wavelength dependent quantities can be computed using the Mie theory provided the aerosol size distribution and complex refractive index are known.

[13] The purpose of this section is to assess such parameters from remote sensing techniques. At a local scale, the single scattering albedo is derived from actinic flux measurements. This parameter is also derived from comparison of airborne flux and aerosol optical thickness measurements in the NIO. The phase function is evaluated through the asymmetry parameter measured at the ground level by an integrating nephelometer. The aerosol optical thickness is measured by mean of an automatic Sun tracking photometer at the ground-based station. Subsequently, the spatial pattern of the AOT is derived at a regional scale from airborne lidar sounding and satellite remote sensing.

3.1. Local-Scale Retrieval of the Aerosol Optical Parameters

3.1.1. Aerosol Optical Thickness

[14] The aerosol optical thickness (AOT) is measured with the help of the Sun photometer following the well-known Bouguer-Langley method.

$$\mathrm{AOT}(\lambda) = \log(\mathrm{E}_0(\lambda)/\mathrm{E}(\lambda))/\mathrm{m} \quad (1)$$

[15] $\mathrm{E}_0(\lambda)$ is the solar top-of-atmosphere (TOA) radiance at wavelength λ. $\mathrm{E}(\lambda)$ is the radiance received by filtered detectors and m is the air mass. The variation in $\mathrm{E}_0(\lambda)$ due to variation of the Sun-Earth distance is taken into account [*Lenoble*, 1993]. The AOT was retrieved based on a careful instrument calibration performed following the method developed by *Herman et al.* [1981]. For the range of AOT observed, the absolute accuracy on the AOT is 0.02 [*Hamonou et al.*, 1999]. The Angström exponent [*Angström*, 1964] is calculated between 440 and 875 nm channels. AOT measured during the field campaign increases from 0.16 (at a wavelength of 550 nm) in late December to 0.83 in early April while the Angström exponent is fairly constant with an average value of 1.40 ± 0.15 over the operating [*Léon et al.*, 2001]. Mean daily AOT (at 440 nm) and Angström exponent obtained between 11 March and 23 March, during the period when the three ground-based instruments used in this paper were working together are displayed on Figures 1a and 1b respectively. A small decrease in the trend of the Angtröm exponent is observed over the 13 days when AOT increases from about 0.70 to 0.85.

3.1.2. Asymmetry Parameter

[16] The angular distribution of the scattered radiation can be computed from the Mie theory when the aerosol size distribution and complex refractive index are known. Nevertheless, it is here convenient to approximate the realistic Mie phase function by a Henyey-Greenstein phase function $\mathbf{p}_{\mathrm{HG}}(\lambda, \Theta)$, with the aerosol asymmetry parameter (hereafter referred as g) as a single free parameter. λ is the wavelength and Θ is the scattering angle. $g(\lambda)$ is in fact an average cosine of the scattering angle weighted by the phase function:

$$\boldsymbol{g}(\lambda) = \frac{1}{2}\int_0^{180} \cos(\Theta)\boldsymbol{p}(\lambda,\Theta)\sin(\Theta)\boldsymbol{d}\Theta \quad (2)$$

And the Henyey-Greenstein phase function $\mathbf{p}_{\mathrm{HG}}(\lambda, \Theta)$ is then given by

$$\boldsymbol{P_{HG}}(\lambda,\Theta) = \left(1-\boldsymbol{g}(\lambda)^2\right)/\left(1+\boldsymbol{g}(\lambda)^2-2\boldsymbol{g}(\lambda)\cos(\Theta)\right)^{3/2} \quad (3)$$

[17] This approximation can result in significant errors when radiances are being computed but it is generally considered acceptable for flux calculations. Nevertheless, it can introduce significant errors (up to 20%) when computing aerosol shortwave radiative forcing [*Boucher*, 1998]. However, for small size distributions (mean geo-

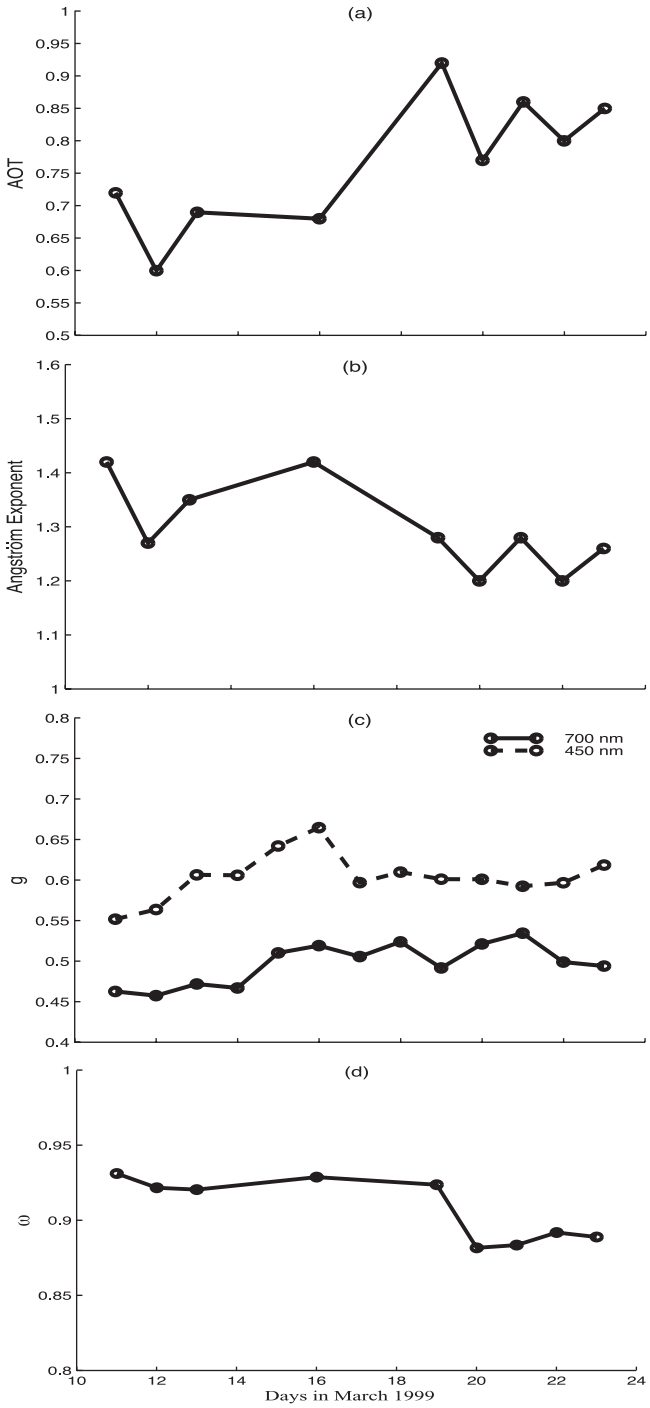

Figure 1. Aerosol optical parameters derived from ground-based measurements. (a) Aerosol optical thickness; (b) Angström exponent; (c) Asymmetry parameter; (d) JNO2-derived single scattering albedo.

metric volume diameter ≤ 0.2 μm) as observed in the NIO [*Satheesh et al.*, 1999; S. C. Alfaro et al., submitted manuscript, 2002], the relative error in the estimate of the aerosol forcing using Henyey-Greenstein and a predicted Mie phase function should be less than 3% [*Boucher*, 1998].

[18] We assess g(λ) through the measurements performed with the integrating nephelometer. Indeed, the ratio R(λ) of the pseudo-back to the pseudo-total scatter measured by the nephelometer at the wavelength λ is related to the aerosol scattering phase function p(λ, Θ) by

$$\boldsymbol{R}(\lambda) = \int_{90}^{170} \boldsymbol{p}(\lambda,\Theta)\sin(\Theta)\boldsymbol{d}\Theta \Big/ \int_{7}^{170} \boldsymbol{p}(\lambda,\Theta)\sin(\Theta)\boldsymbol{d}\Theta \quad (4)$$

[19] g(λ) is derived at 450 and 700 nm by minimizing (in a least squares meaning) the difference between nephelometer measurements of R(λ) and computed values using equations (3) and (4) for various asymmetry parameters.

[20] Backscatter and total scatter nephelometric coefficients are measured every 10 s and averaged over 1 minute which leads to a relative spread on g(λ) below 9%. The daily variability of R(λ) is less than 15 % over the 13 days of measurement. Over the operating period, derived values of R(λ) are ranging between 0.53 and 0.66 at 450 nm and between 0.48 and 0.53 at 700 nm. The associated mean asymmetry parameters are 0.49 ± 0.02 and 0.60 ± 0.03 in the red and in the blue channel respectively. The temporal evolution of g is plotted on Figure 1c. No significant trend is observed during the operating period.

[21] We can compare the derived values of g with other values obtained during field experiments. In the visible spectrum, the spectral dependency of g is linear [see *Ross and Hobbs*, 1998]. At 0.55 μm (which can be used as a reference for the visible spectrum), we have 0.53 ± 0.03. As a comparison, *Ross and Hobbs* [1998] find g ≈ 0.54 during SCAR-B (Smoke clouds and radiation-Brazil [*Kaufman et al.*, 1998]) experiment for biomass burning aerosols using a closure test experiment. On the other hand, during the Tropospheric Aerosol Radiative Forcing Observational eXperiment (TARFOX), *Hignett et al.* [1999] derive g = 0.58 for pollution aerosols from the Northeast U.S. Those two literature values were obtained by measuring the size distribution and assessing the complex refractive index from aerosol chemical analysis. In this study, we have estimated g by mean of optical measurements. Our value is coherent with other studies dealing with anthropogenic aerosols.

3.1.3. Single Scattering Albedo

[22] Many methods exist to measure directly the aerosol single scattering albedo (cf. *Heitzenberg et al.* [1997] for a

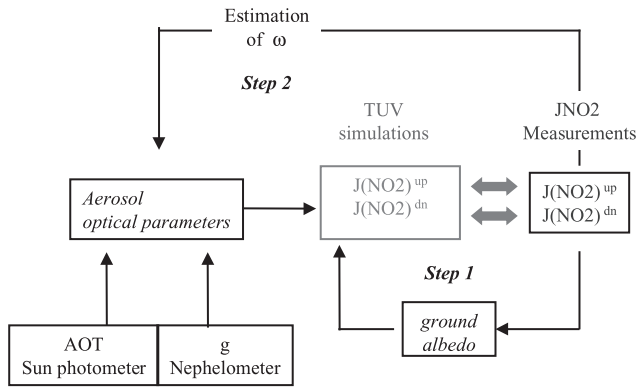

Figure 2. Overview of the iterative procedure used for the assessment of the aerosol single scattering albedo from JNO2 measurements.

review). We propose here an inverse method based on actinic flux measurements and radiative transfer simulation. The radiative transfer code used is the Tropospheric Ultraviolet and Visible code (TUV Version 4.0 developed by *Madronich* [1987] and available at http://acd.ucar.edu). This code is well dedicated to photolysis rate computation and allows one to interpret directly JNO2 measurements. The parametric scheme used to solve the radiative transfer equation is the pseudo-spherical n-stream discrete ordinate method [*Stamnes et al.*, 1988; *Zeng et al.*, 1996]. Figure 2 gives an overview of the iterative procedure used in the following. Input parameters of the simulation are the aerosol optical parameters and the ground surface albedo. AOT and g are known from the photometer and the nephelometer, respectively. Output parameters are $J(NO_2)^{up}$ and $J(NO_2)^{dn}$ which are iteratively compared to measurements to constrain the two parameters (ground albedo and aerosol single scattering albedo).

[23] In a first step, the plane surface albedo is derived using the measured ratio of $J(NO_2)^{up}$ to $J(NO_2)^{dn}$. The plane albedo is defined as the ratio of the upward irradiance to the upward irradiance at the ground level. $J(NO_2)^{up}/J(NO_2)^{dn}$ is not directly related to the plane albedo but a linear relationship can be derived between the both. We assume that the ground albedo follows the Lambert's law and to reduce bidirectional ground effects, all the following measurements are performed at the same solar zenith angle, close to 27°. Over the 4 available days, the measured ratio is 0.13 (±0.01). The iterative comparison between simulated and measured $J(NO_2)^{up}/J(NO_2)^{dn}$ leads to a plane surface albedo of 0.10 (±0.01). The standard deviations given in brackets are due to the measurement variability.

[24] In a second step, we use $J(NO_2)^{up}$ to derive ω so that the effect of the ground albedo is of the second order. The variability of ±0.01 in the derived plane surface albedo leads to an uncertainty below 1% on simulated $J(NO_2)^{up}$. The TUV code is run for different values of the aerosol single scattering albedo (hereafter referred as ω) and g. On Figure 3, the NO_2 photolytis rate is plotted as a function of the AOT for different values of ω and g. The retained ranges of ω (0.8–0.95 at 440 nm) and g (0.5–0.7 at 440 nm) are typical of moderate absorbing anthropogenic aerosols [*D'Almeida et al.*, 1991] as it could be expected in the INDOEX plume [*Satheesh et al.*, 1999]. Moreover, the 0.5–0.7 g range include the value we have derived at the ground thanks to the nephelometer. At the ground level $J(NO_2)$ is a decreasing function of the AOT and an increasing function of ω. For a given AOT, matching the measured $J(NO_2)$ leads to a possible couple of g and ω. The AOT is provided by the Sun photometer and we have used the nephelometer derived-g value as a first estimate. As an example taken for 11 March, simulation of $J(NO_2)$ is plotted as a function of ω on Figure 4. The two curves represent the upper and lower bounds regarding the uncertainty on the AOT retrieval for 11 March and the 0.5–0.7 asymmetry parameter range. The accuracy in $J(NO_2)$ is displayed as horizontal lines. The projection on the ω-axis gives the uncertainty on the retrieved ω value. Then the expected absolute uncertainty on the retrieved ω is less than 0.04 whatever is the value of g.

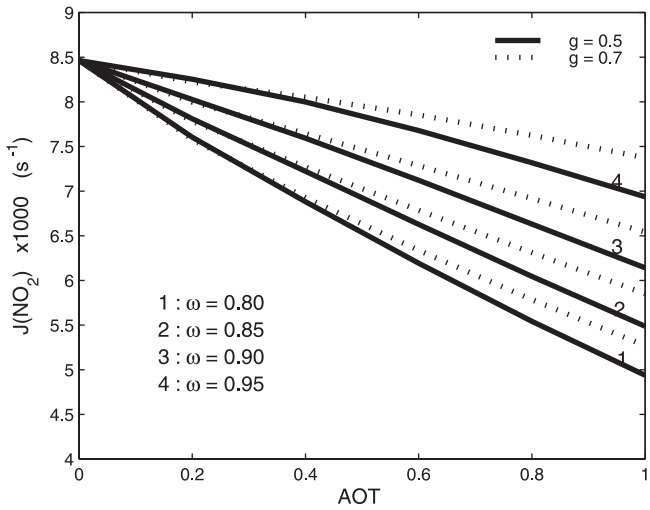

Figure 3. Simulated $J(NO_2)$ as a function of the AOT for different values of the aerosol single scattering albedo and asymmetry parameter.

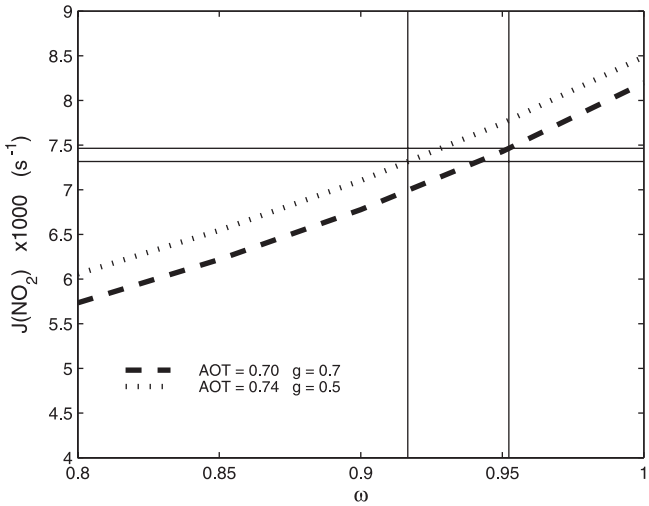

Figure 4. Simulated $J(NO_2)$ as a function of the aerosol single scattering albedo.

[25] We have retained only the 9 cloud free days (i.e., clear upward hemisphere during the day) between 11 March and 23 March. The corresponding coincident measurements obtained by the Sun photometer, the nephelometer, and the optical actinometer and used in the computation are displayed on Figures 1a, 1b, and 1c. Missing data correspond to cloudy days. The derived values of ω are presented in Figure 1d. Maximum and minimum encountered values are 0.93 and 0.88 respectively. The average value is 0.90 ± 0.02. We can observe 2 different periods before and after 20 March. The change in ω is nearly simultaneous with the increase in AOT. This feature may be linked with a change in the atmospheric circulation as it has been shown by *Léon et al.* [2001] (cf. Figure 10).

[26] Between 20 and 26 March, (S.C. Alfaro, university of Paris 12, personal communication, 2002) have derived from ground-based closure experiment a single scattering albedo at 0.89 at 50% of relative humidity. This value was found coherent with Sun photometer-derived single scatter-

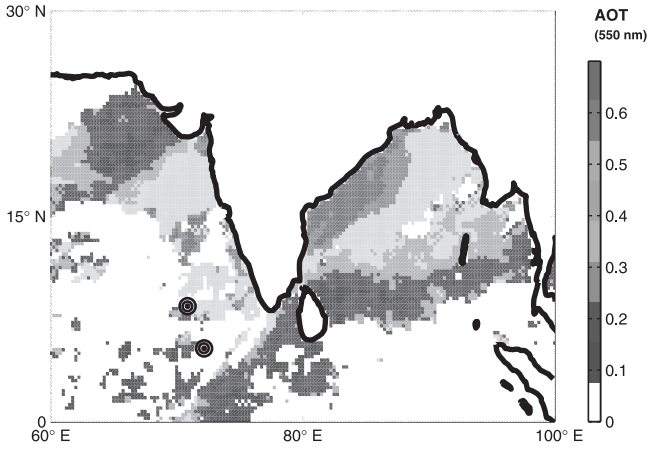

Figure 5. Meteosat-5-derived AOT for March 9, 1999. Black dots correspond to M20 acquisitions.

ing albedo using the method proposed by *Dubovik et al.* [1998] and available on the AERONET (Aerosol Robotic Network) database. This value is also coherent with the one we derive using the optical actinometer in late March. Summing up several independent measurements performed in the NIO, *Ramanathan et al.* [2001], propose a value for the columnar ω between 0.86 and 0.90 in agreement with our results.

3.2. Columnar and Regional Aerosol Characteristics

3.2.1. Meteosat AOT

[27] Retrieval of AOT from spaceborne radiometer requires a priori knowledge of the aerosol optical properties. The choice of this model results from both ground in situ analysis (S. C. Alfaro et al., submitted manuscript) and comparison of Meteosat-derived AOT with Sun photometer measurements performed at the Goa experimental site [*Léon et al.*, 2001]. A monomodal lognormal size distribution with a mean radius of 0.06 μm (standard deviation of 1.72) and a complex refractive index of 1.43 – i0.03 were found to best fit ground-based measurements. The Meteosat-5-derived AOT has also been compared with AOT measurements performed during the 1999 cruise of the Sagar Kanya Indian oceanographic research vessel. The agreement between spaceborne and shipborne AOT indicates that the aerosol model used for Meteosat-5 analysis should be representative of the aerosol advected from India over the Arabian Sea. The $g(\lambda)$ derived from the Meteosat model and using Mie theory are 0.50 and 0.63 at 700 and 450 nm respectively. ω is 0.83 at 550 nm. These values are in a good agreement with our present results.

[28] Figure 5 is a map of AOT derived from Meteosat-5 visible channel on 9 March corresponding to the M20 acquisitions discussed hereafter. White areas correspond to land and cloud masking. Many clouds inside the plume disable AOT inversion. However, AOT is ranging between 0.5 and 0.6 inside the plume spreading from the Indian coast to the Arabian Sea. Outside the plume, below the tip of India, AOT is ranging between 0.1 and 0.2.

3.2.2. Lidar Profiles

[29] Vertical profiles of the aerosol extinction coefficient has been derived from LEANDRE-1 backscattered lidar signal. Lidar signal were inverted using a constant value with altitude of the backscatter-to-extinction ratio of $0.012 sr^{-1}$ in the forward *Klett* [1985] algorithm (see also *Flamant et al.* [1998]). This value has been derived from comparison with lidar integrated AOT and Sun photometer AOT at Kaashidoo (Maldives republic) observatory [*Chazette et al.*, 1999].

[30] We present here two profiles obtained during the IFP. The first one is characteristic of the aerosol plume spreading from the west coast of India over the ocean. The second one is characteristic of the aerosol condition prevailing outside the Indian plume (see also *Pelon et al.* [2000]). Figure 6a displays vertical profiles of the aerosol extinction coefficients obtained at the two different locations reported on Figure 5 as black dots. Plain line corresponds to a location at (5.35°N, 72.16°E) near the Maldives Islands (outside the monsoon layer aerosol plume) and dashed line is at (8.43°N, 70.85°E) southwest of Goa (inside the aerosol plume).

[31] Outside the plume (plain line), a 2-layer structure can be observed: a Marine Boundary Layer (MBL) with increasing extinction coefficient from 0.1 km^{-1} to 0.2 km^{-1} at ~500 m topped by the free troposphere with an extinction coefficient decreasing toward 0 km^{-1} at 2 km above sea level. Total AOT is 0.16 for this profile. It is very similar to the one observed by *Livingston et al.* [2000] during the 2nd aerosol characterization experiment (ACE-2) in the atmos-

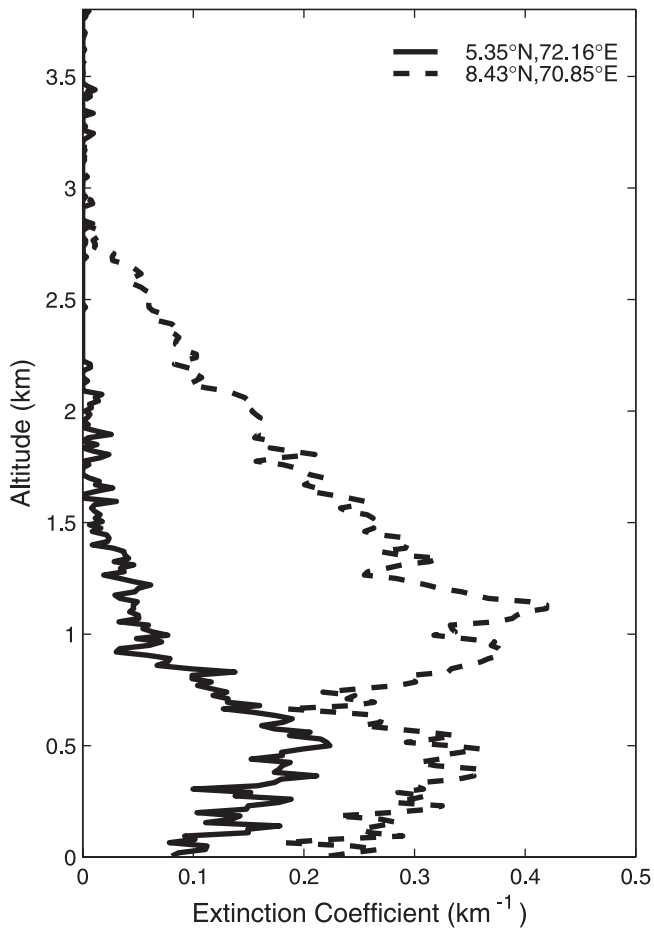

Figure 6. Vertical profile of the aerosol extinction coefficient derived from lidar sounding on 9 March 1999.

Table 1. Reflectance Above the Aerosol Measured by Airborne Devices[a]

Location of Acquisition	Solar Zenith Angle	Integrated AOT (532 nm)	R_a
(5.35°N, 72.16°E)	20.0°	0.16	6.48×10^{-2}
(8.43°N, 70.85°E)	32.2°	0.61	9.18×10^{-2}

[a] AOT is integrated using the aerosol extinction vertical profile derived from the lidar signal.

phere of the North Atlantic. This profile is representative of an anthropogenically modified (polluted) MBL.

[32] For the second profile (dashed line) the shape is very similar to the first one up to 700 m but with an aerosol extinction value 1.75 times higher. From 700 m to 1.2 km the extinction coefficient increases again and above 1.2 km it decreases from 0.4 to 0 km^{-1} above 3 km. The associated AOT is 0.61. The contribution of the layer observed over the MBL to the total AOT is then close to 74%. This contribution is due to the advection of continental air masses from India in the winter monsoonal pollution layer as pointed out by [*Léon et al.*, 2001].

[33] Airborne lidar and satellite observations confirm the presence of a well geographically-defined aerosol layer spreading over the NIO from the west Indian coast (see also *Rasch et al.* [2001], *Ramanathan et al.* [2001], and *Léon et al.* [2001]). In the following, we focus on the radiative characteristics of this layer.

3.2.3. Flux Measurements

[34] At the top of the aerosol layer, the reflectance of the underlying atmosphere R_a is the ratio of the upward to the downward fluxes. This ratio was measured at about 6 km height by use of the two Eppley pyranometers on board M20. Measurements are summed up in Table 1. The expected accuracy is ±2%. We have simulated this ratio using the Streamer radiative transfer code [see *Key*, 1999, and reference therein], itself based on the discrete ordinate method [*Stamnes et al.*, 1988]. The surface albedo used is an ocean reflectance wavelength independent empirical model given by *Briegleb et al.* [1986]. In our simulation, the vertical profile of extinction coefficient (Figure 6) derived from each lidar sounding is taken as input. In the simulation, we let ω as a degree of freedom. The aerosol optical parameter wavelength dependency is the same as for the Meteosat-5 model.

[35] R_a is matched inside and outside the plume when the fitted value of the single scattering albedo are 0.83 (±0.05) and 0.87 (±0.1) respectively. This is in the range of the value derived at the Goa university. Moreover 0.83 is the value used for Meteosat-5 analysis.

[36] *Ramanathan et al.* [2001] point out a decrease in ω between the MBL and the MBL topped by the monsoon layer (ML). Indeed, their measurements show a difference between the surface where ω ranges between 0.85 and 0.90 and above the surface layer where ω ranges between 0.8 and 0.90. With a six-wavelength lidar at Hululé (Maldives international airport), *Ansmann et al.* [2000] assessed a ω between 0.75 and 0.9 inside the Monsoon layer. This could be expected since the profile derived outside the plume is likely a mixing between natural background non absorbing (oceanic) and anthropogenic aerosols. However, the accuracy in the single scattering albedo of the polluted MBL is too weak to estimate this parameter for the ML.

4. Shortwave Radiative Forcing

[37] Aerosol clear sky (cloud free) radiative forcing is defined as the difference in the net flux (downward minus upward fluxes) between an atmosphere with and without aerosols. The aerosol effect is then estimated through the aerosol forcing efficiency, f, which is the change in the net flux per unit of AOT. Hereafter, f_{TOA} and f_{surf} stand for the diurnal average of the top-of-atmosphere (TOA) and surface forcing efficiencies. The difference between both is the atmosphere forcing efficiency f_{atm} which can be expressed as a diurnal mean heating rate perturbation when the vertical range of the aerosol layer is known.

[38] In this section, we estimate the aerosol clear sky radiative impact. For this purpose, the vertical and the geographical distribution of the pollution layer are assessed by use of airborne lidar sounding and Meteosat-5 imagery. The profile outside the plume is likely a mixing between natural background (oceanic) and anthropogenic aerosols. In the following computations, we assumed that the visible AOT background aerosol is 0.07 which is an average value compared to the premonsoonal daily mean value ranging between 0.05 and 0.1 prevailing in the NIO [*Ramanathan et al.*, 2001]. The background aerosol optical properties are modeled using a maritime aerosol model [*Shettle and Fenn*, 1979]. The relative vertical distribution is the same as for the lidar profile outside the plume (see Figure 6) and is averaged every 100 m.

[39] The aerosol optical model derived in the previous section is used as input for the computation of radiative forcing from anthropogenic aerosols. Computations are performed for two values of single scattering albedo. ω = 0.83 corresponds to a lower limit for the estimation performed at the Goa station and has been found in a good agreement with M20 flux measurements. ω = 0.90 corresponds to the average value observed during the operating period in March 1999 at the Goa station.

4.1. Aerosol Radiative Forcing at a Regional Scale

[40] To provide a regional scale evaluation of the direct radiative forcing at the TOA (ΔF_{TOA}) and at the surface (ΔF_{surf}), we have used the AOT derived from Meteosat-5 visible channel. The daily shortwave radiative forcing is then assessed by multiplying the forcing efficiency for the TOA and surface respectively. Mean daily forcing efficiency estimations are presented in Table 2. Shifting ω from 0.83 to 0.90 leads to an (absolute) increase in the TOA forcing efficiency by 9 W m^{-2} whereas the surface forcing decreases by 12 W m^{-2}. Taking into account the accuracy

Table 2. Surface (f_{surf}), TOA (f_{TOA}), and Atmospheric (f_{atm}) Shortwave Radiative Forcing Efficiency for Two Values of the Single Scattering Albedo (ω)

	Forcing Efficiency, W m^{-2}		
ω	f_{surf}	f_{TOA}	f_{atm}
0.83	−84	−18	66
0.9	−72	−27	45

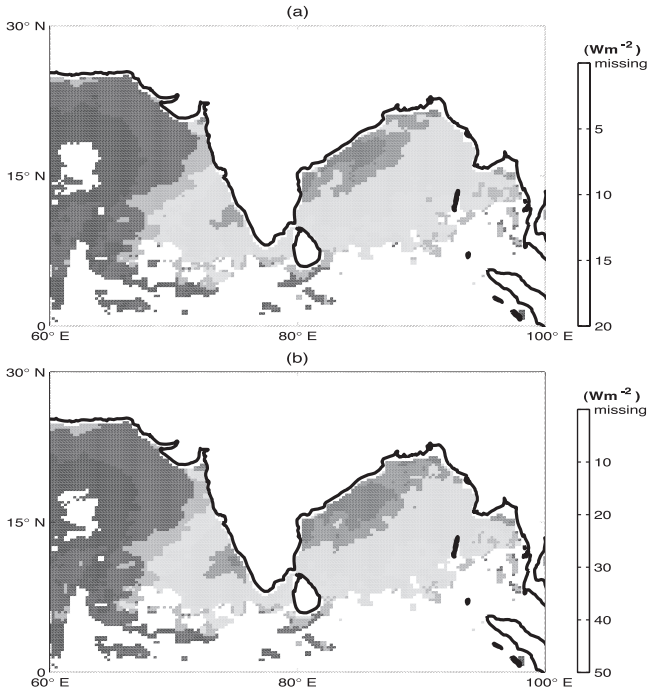

Figure 7. Mean daily shortwave direct aerosol forcing for the last period of ten days of March, 1999. (a) at the TOA. (b) at the surface.

on the Meteosat retrieved AOT (≈25% [*Moulin et al.*, 1997]), we can estimate the forcing with a an accuracy close to 30%. *Satheesh and Ramanathan* [2000] give for February–March 1998 and 1999, $f_{TOA} \approx -25$ W m^{-2} and $f_{surf} \approx -75$ W m^{-2} using calibrated satellite radiation measurements and surface radiometers. *Podgorny et al.* [2000] have computed from the *Satheesh et al.* [1999] model, $f_{TOA} \approx -20$ W m^{-2} and $f_{surf} \approx -82$ W m^{-2}. Our present results $\sim f_{TOA} \approx -22$ W m^{-2} and $f_{surf} \approx -78$ W m^{-2}) confirm that those forcing efficiencies are representative of the polluted NIO.

[41] We present on Figure 7 the regional distribution of the mean daily shortwave radiative forcing for the last period of ten days of March, 1999. This period corresponds to a maximum in AOT over the NIO [see *Léon et al.*, 2001, Figure 10d]. Moreover, the measurements performed at Goa and analyzed previously have been realized during this period. ΔF_{TOA} and ΔF_{surf} are then estimated with ω = 0.90 corresponding to the average value derived at the Goa station during this period (Figure 1d). Figure 7a is for TOA forcing and Figure 7b for the surface forcing. Inside the plume spreading from India (mean AOT ≈ 0.6), we estimate the shortwave radiative forcing $\Delta F_{TOA} = -17$ (±5) W m^{-2}, $\Delta F_{surf} = -45$ (±13) W m^{-2}. The quantities inside the brackets corresponds to the estimated uncertainties taking into account the accuracy for the AOT retrieval method (≈25%) and the effect of the uncertainty on ω (≈15%). The radiative forcing is also displayed over the Bay of Bengal. Indeed, due to the similarity of aerosol sources (G. Cautenet et al., unpublished manuscript, 2000) we could expect that the shortwave computation performed for the Arabian Sea also apply to the Bay of Bengal.

[42] The estimated forcing are in the same order of magnitude of previous estimations for different regions. During SCAR-B experiment, for biomass burning by-products aerosols, *Ross and Hobbs* [1998] have estimated, a daily averaged TOA radiative forcing of -26 ± 6 W m^{-2} (AOT = 1.0 at 550 nm) for SCAR-B aerosols over ocean surface. During the Tropospheric Aerosol Radiative Forcing Observational eXperiment (TARFOX), for an typical AOT of 0.3 (550 nm) *Hignett et al.* [1999] give a value of -9 W m^{-2} and -26 W m^{-2} for the TOA and the surface forcing respectively. In those experiments as for the INDOEX case, the presence of soot aerosols is responsible for the multiplying factor between the TOA and the surface forcing. We report here a value between 2.5 and 4.5 for this factor. *Satheesh and Ramanathan* [2000] have found a multiplying factor of ~3 for the period February–March 1998 and 1999. The difference between ΔF_{TOA} and ΔF_{surf} correspond to the atmospheric forcing which induces a heating of the aerosol layer. We have investigated the vertical range of this heating thanks to the lidar soundings.

4.2. Shortwave Atmospheric Heating Rate

[43] On Figures 8a and 8b, diurnal shortwave atmospheric radiative heating rates estimated from lidar soundings are plotted as a function of the altitude for the two values of ω. Figure 8b corresponds to the anthropogenically modified MBL and Figure 8a to the presence of the ML in the Arabian Sea. Over the first 3 km of the atmosphere, the average heating rate is 0.21 ± 0.05 Kd^{-1} outside the plume and 1.0 ± 0.2 Kd^{-1} for the profile inside the plume. As a comparison, in a desert dust outbreak off the Sahel region, *Fouquart et al.* [1987] have reported a daily averaged shortwave heating rate of 1.8 Kd^{-1} for an AOT of 1.5. For the INDOEX case, when the AOT is scaled to reach unity, the atmospheric heating rate is between 1.78 Kd^{-1} (for ω = 0.83) and 1.22 Kd^{-1} (for ω = 0.90). This means that the anthropogenic aerosols significantly impact the atmospheric radiative heating budget even their associated AOT is less than for dust events.

[44] The most important feature is the vertical distribution of this heating. Maximum heating (up to 2.2 Kd^{-1}) occurs at about 1 km height inside the plume due to the presence of the ML. Such a modification of the energetic balance of the atmosphere could have significant impact either on the dynamics or water cycle in the tropical atmosphere. Indeed, *Ackerman et al.* [2000] have demonstrated that the heating effect could impact cloudiness by clearing trade cumulus at this altitude. At a regional scale, this semidirect effect could then off-set the radiative cooling at the TOA induced by aerosols [*Ackerman et al.*, 2000]. Moreover, the vertical gradient of expected heating rate in the atmosphere could enhance the stability of the ML and thus increase the residence time of aerosol in the ML enhancing the large scale advection of anthropogenic aerosols toward the South Indian ocean.

5. Summary and Conclusion

[45] In this paper, we have assessed the shortwave direct aerosol effect of the Indo-Asian haze spreading over the NIO during the winter-dry monsoon. A particular attention has been paid to the impact of the haze on the vertical

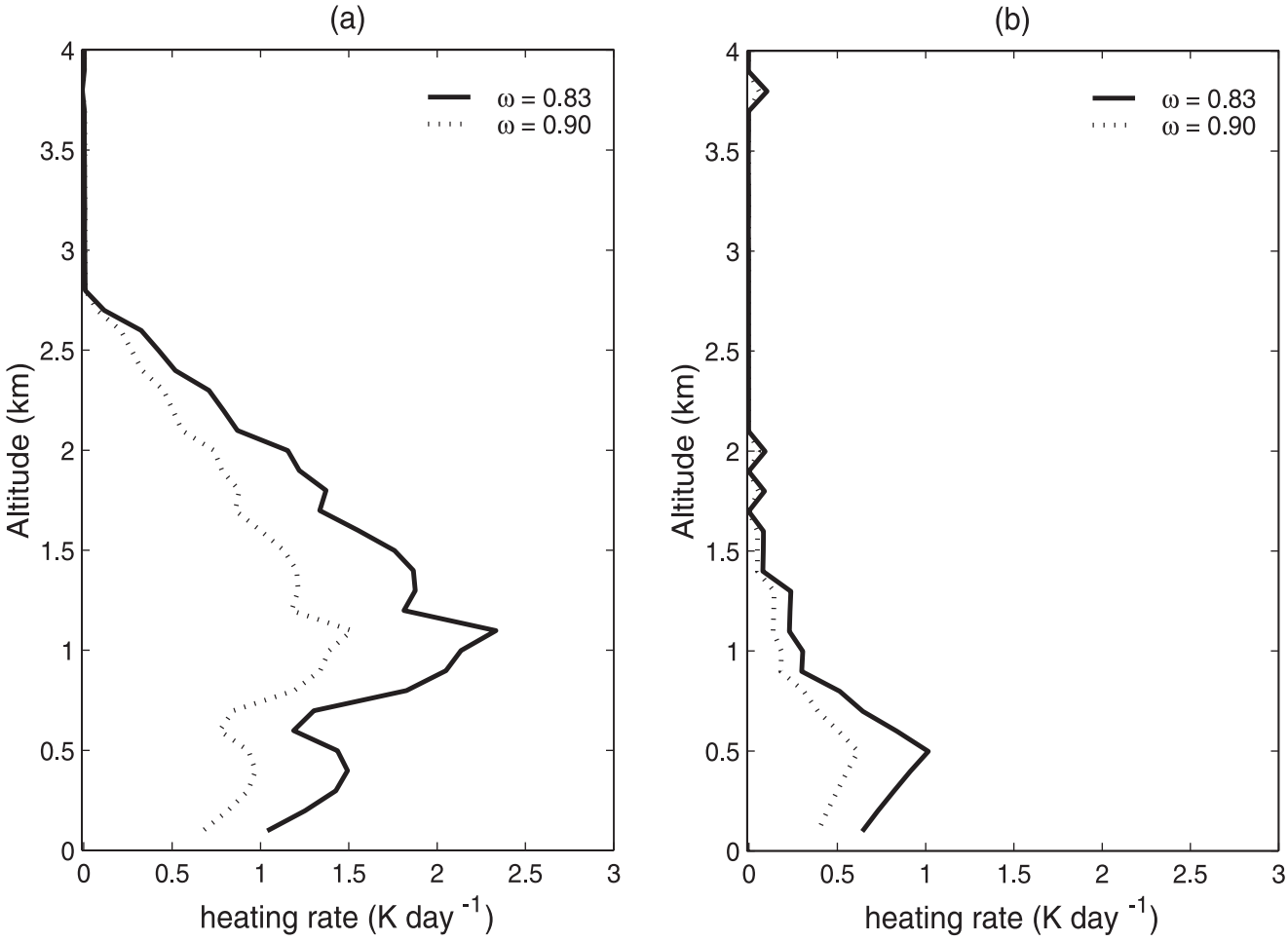

Figure 8. Vertical range of the additional shortwave atmospheric heating rate. (a) location corresponds to (8.43°N, 70.85°E). (b) Location corresponds to (5.35°N, 72.16°E).

radiative budget of the atmosphere. The aerosol optical parameters required for the aerosol shortwave forcing assessment have been evaluated at the Goa experimental site in March 1999 by use of an instrumental synergy. We have mainly focused on the estimation of the aerosol single scattering albedo. For this purpose, we have developed an original method based on actinic flux measurements at the Goa station. The single scattering albedo has been found to range between 0.88 ± 0.04 and 0.93 ± 0.04 between 11 March and 23 March. Moreover, we have also assessed this parameter of the Indian by comparing simultaneous airborne lidar and flux measurements with radiative transfer simulations. The value retrieved for the atmospheric column is 0.83. Those values are in a good agreement with the one used in the Meteosat-5 AOT analysis (0.83).

[46] From satellite monitoring of the aerosol optical thickness, we have also presented the geographical distribution of the expected aerosol forcing in terms of TOA, surface and atmospheric forcing. Moreover, we have derived from lidar airborne sounding the direct shortwave atmospheric heating rate as a function of the altitude. The vertical energy budget of the lowest 3 km of the atmosphere is affected by the presence of the haze layer which induces heating. The maximum heating ($\approx$2.2 Kd^{-1}) is close to 1 km height where. It is suggested that this additional heating could significantly impact the dynamics and water budget of the atmosphere and then the lapse rate of aerosols in the low troposphere.

[47] **Acknowledgments.** This work is sponsored by INSU/CNRS "Programme National de Chimie Atmosphérique." The authors wish to thank Gilles Bergametti for helpful discussion.This is the LSCE contribution 0648.

References

Ackerman, A. S., O. S. Toon, D. E. Stevens, A. J. Heymsfield, V. Ramanathan, and E. J. Welton, Reduction of tropical cloudiness by soot, *Science*, *288*, 1042–1047, 2000.

Alpert, P., Y. J. Kaufman, Y. Shay-El, D. Tanré, A. Da silva, S. Schubert, and J. H. Joseph, Quantification of dust-forced heating of the lower troposphere, *Nature*, *395*, 367–370, 1998.

Angström, A., The parameters of atmospherics turbidity, *Tellus*, *16*, 64–75, 1964.

Ansmann, A., D. Althausen, U. Wandingen, K. Franke, D. Müller, F. Wagner, and J. Heitzenberg, Vertical profiling of the Indian aerosol plume with six-wavelength lidar during INDOEX: A first case study, *Geophys. Res. Lett.*, *27*, 963–966, 2000.

Boucher, O., On aerosol direct shortwave forcing and the Henyey-Greenstein phase function, *J. Atmos. Sci.*, *55*, 128–134, 1998.

Briegleb, B. P., P. Minnis, V. Ramanathan, and E. Harrison, Comparison of regional clear-sky albedos inferred from satellite observations and model computations, *J. Clim. Appl. Meteorol.*, *25*, 214–226, 1986.

Charlson, R. J., S. E. Schwartz, J. M. Hales, R. D. Cess, J. J. A. Coakley,

J. E. Hansen, and D. J. Hofmann, Climate forcing by anthropogenic aerosols, *Science*, *255*, 423–430, 1992.

Chazette, P., et al., Micropulse lidar to retrieve the structural and optical properties of the aerosols in the frame of INDOEX campaign, *Eos Trans. AGU80*(46), Fall Meet. Suppl., F164, 1999.

Chylek, P., G. Videen, D. Ngo, R. G. Pinnick, and J. D. Klett, Effect of black carbon on the optical properties and climate forcing of sulfate aerosols, *J. Geophys. Res.*, *100*, 16,325–16,332, 1995.

D'Almeida, G. A., P. Koepke, and E. P. Shettle, *Atmospheric Aerosols*, A. Deepak, Hampton, Va., 1991.

Dubovik, O., B. N. Holben, Y. J. Kaufman, M. Yamasoe, A. Smirnov, D. Tanré, and I. Slutsker, Single scattering albedo of smoke retrieved from sky radiance and solar transmittance measured from ground, *J. Geophys. Res.*, *103*, 31,903–31,923, 1998.

Dulac, F., D. Tanré, G. Bergametti, P. Buat-Ménard, M. Desbois, and D. Sutton, Assessment of the African airborne dust mass over the western Mediterranean Sea using Meteosat data, *J. Geophys. Res.*, *97*, 2489–2506, 1992.

Flamant, C., V. Trouillet, P. Chazette, and J. Pelon, Wind speed dependence of atmospheric boundary layer optical properties and ocean surface reflectance as observed by airborne backscatter lidar, *J. Geophys. Res.*, *103*, 25,137–25,158, 1998.

Fouquart, Y., B. Bonnel, G. Brogniez, J. C. Buriez, L. Smith, J. J. Morcrette, and A. Cerf, Observations of Saharan aerosols: Results of ECLATS field experiment, part II, Broadband radiative characteristics of the aerosols and vertical radiative flux divergence, *J. Clim. Appl. Meteor.*, *26*, 38–52, 1987.

Fraser, R. S., Satellite measurement of mass of Sahara dust in the atmosphere, *Appl. Opt.*, *15*, 2471–2479, 1976.

Hamonou, E., P. Chazette, D. Balis, F. Dulac, X. Schneider, E. Galani, G. Ancellet, and A. Papayannis, Characterisation of the vertical structure of Saharan dust export to the Mediterranean basin, *J. Geophys. Res.*, *104*, 22,257–22,270, 1999.

Harshvardhan, Aerosol climate interactions, in *Aerosol-Cloud-Climate Interactions*, edited by P. V. Hobbs, pp. 75–95, Academic, San Diego, Calif., 1993.

Haywood, J., and O. Boucher, Estimates of the direct and indirect radiative forcing due to tropospheric aerosols: A review, *Rev. Geophys.*, *38*, 513–543, 2000.

Heitzenberg, J., R. J. Charlson, A. D. Clarke, C. Liousse, V. Ramaswamy, K. P. Shine, M. Wendish, and G. Helas, Measurements and modelling of aerosol single-scattering albedo: progress, problems and propects, *Beitr. Phys. Atmos.*, *70*, 249–263, 1997.

Herman, B. M., M. A. Box, J. A. Reagan, and C. M. Evans, Alternate approach to the analysis of solar photometer data, *Appl. Opt.*, *20*(17), 2925–2928, 1981.

Hignett, P., J. P. Taylor, P. N. Francis, and M. D. Glew, Comparison of observed and modeled direct forcing during TARFOX, *J. Geophys. Res.*, *104*, 2279–2287, 1999.

Holben, B. N., et al., AERONET-A federated instrument network and data archive for aerosol characterisation, *Remote Sens. Environ.*, *66*, 1–16, 1998.

Jankowiak, I., and D. Tanré, Satellite climatology of Saharan dust outbreaks: Method and preliminary results, *J. Clim.*, *5*, 646–656, 1992.

Kaufman, Y. J., D. Tanré, H. R. Gordon, T. Nakajima, J. Lenoble, R. Frouin, H. Grassl, B. M. Herman, M. D. King, and P. M. Teillet, Passive remote sensing of tropospheric aerosol and atmospheric correction for the aerosol effect, *J. Geophys. Res.*, *102*, 16,815–16,830, 1997.

Kaufman, Y. J., et al., Smoke, Clouds, and Radiation-Brazil (SCAR-B) experiment, *J. Geophys. Res.*, *103*, 31,783–31,808, 1998.

Key, J., Streamer user's guide, 90 pp., Dep. of Geogr., Boston Univ., Boston, Mass., 1999.

Kiehl, J. T., and B. P. Briegleb, The relative roles of sulfate aerosols and greenhouse gases in climate forcing, *Science*, *260*, 311–314, 1993.

Klett, J. D., Lidar inversion with variable backscatter/extinction ratios, *Appl. Opt.*, *24*, 1638–1643, 1985.

Lenoble, J., *Atmospheric Radiative Transfer*, A. Deepak, Hampton, Va., 1993.

Léon, J.-F., et al., Large scale advection of continental aerosols during INDOEX, *J. Geophys. Res.*, *106*, 28,427–28,440, 2001.

Livingston, J. M., et al., Shipborne sunphotometer measurements of aerosol optical depth spectra and columnar water vapor during ACE-2, and comparison with selected land, ship, aircraft, and satellite measurements, *Tellus, Ser. B*, *52*, 596–619, 2000.

Madronich, S., Photodissociation in the Atmosphere, 1, Actinic flux and effects of ground reflections and clouds, *J. Geophys. Res.*, *92*, 9740–9752, 1987.

Moulin, C., F. Dulac, C. E. Lambert, P. Chazette, I. Jankowiak, B. Chatenet, and F. Lavenu, Long-term daily monitoring of Saharan dust load over ocean using ISCCP-B2 data, 2, Accuracy of the method and validation using Sun photometer measurements, *J. Geophys. Res.*, *102*, 16,959–16,969, 1997.

Pelon, J., P. Chazette, C. Flamant, J.-F. Léon, D. Tanré, G. Cautenet, M. Sicard, P. Genau, F. Blouzon, and N. Grand, INDOEX campaign, Mystere 20 flights, 35 pp., Institut Pierre Simon Laplace, Paris, 2000.

Pelon, J., P. H. Flamant, and M. Meisonnier, The French airborne backscatter lidar Leandre-1: Conception and operation, paper presented at 15th International Laser Radar Conference, International coordination-group on laser Atmospheric studies, Tomsk, 1990.

Podgorny, I. A., W. Conant, V. Ramanathan, and S. K. Satheesh, Aerosol modulation of atmospheric and surface solar heating over the tropical Indian Ocean, *Tellus, Ser. B*, *52*, 947–958, 2000.

Ramanathan, V., et al., The Indian Ocean Experiment: An integrated assessment of the climate forcing and effects of the great Indo-Asian haze, *J. Geophys. Res.*, *106*, 28,371–28,398, 2001.

Rasch, P. J., W. D. Collins, and B. E. Easton, Understanding the Indian Ocean Experiment (INDOEX) aerosol distributions with an aerosol assimilation, *J. Geophys. Res.*, *106*, 7337–7355, 2001.

Ross, J. L., and P. V. Hobbs, Radiative characteristics of regional hazes dominated by smoke from biomass burning in Brazil: Closure tests and direct radiative forcing, *J. Geophys. Res.*, *103*, 31,925–31,991, 1998.

Russel, P. B., S. A. Kinne, and R. W. Bergstrom, Aerosol climate effects: Local radiative forcing in column closure experiments, *J. Geophys. Res.*, *102*, 9397–9407, 1997.

Satheesh, S. K., and V. Ramanathan, Large difference in tropical aerosol forcing at the top of the atmosphere and Earth's surface, *Nature*, *405*, 60–63, 2000.

Satheesh, S. K., V. Ramanathan, X. Li-Jones, J. M. Lobert, I. A. Podgorny, J. M. Prospero, B. N. Holben, and N. G. Loeb, A model for the natural and anthropogenic aerosols over the tropical Indian Ocean derived from Indian Ocean Experiment data, *J. Geophys. Res.*, *104*, 27,421–27,440, 1999.

Schwartz, S. E., and P. R. Buseck, Absorbing phenomena, *Science*, *288*, 989–990, 2000.

Shettle, E. P., and R. W. Fenn, Models for the aerosols of the lower atmosphere and the effects of humidity variations on their optical properties, AFGL-TR-79-0214, U.S. Air Force Geophys. Lab., Hanscomb, Mass., 1979.

Stamnes, K., S. C. Tsay, W. Wiscombe, and K. Jayaweera, Numerical stable algorithm for discrete-ordinate-method radiative transfer in scattering and emitting layered media, *Appl. Opt.*, *27*, 2502–2509, 1988.

Twomey, S. A., M. Piepgrass, and T. L. Wolfe, An assessment of the impact of pollution on the global cloud albedo, *Tellus, Ser. B*, *36*, 356–366, 1984.

Veefkind, J. P., J. C. H. Van der Hage, and H. M. Ten Brink, Nephelometer derived and directly measured aerosol optical depth of the atmospheric boundary layer, *Atmos. Res.*, *41*, 217–228, 1996.

Zeng, J., S. Madronich, and K. Stammes, A note on the use of the two-stream delta-scaling approximation for calculating atmospheric photolysis rate coefficients, *J. Geophys. Res.*, *101*, 14,525–14,530, 1996.

P. Chazette, F. Dulac, J.-F. Léon, and H. Randriamiarisoa, Laboratoire des Sciences du Climat et de l'Environnement, CEA-CNRS, 91191 Gif/Yvette, Cedex, France.

J. Pelon, Service d'Aéronomie, CNRS-UPMC, Paris, 75252, France.